Acta Materialia 283 (2025) 120515

Contents lists available at ScienceDirect

Acta Materialia

journal homepage: www.elsevier.com/locate/actamat

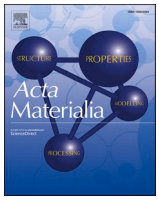

Full length article

Magnetic imaging of thermally switchable antiferromagnetic/ferromagnetic modulated thin films

W. Griggs [a,*], A. Peasey [a], F. Schedin [b], Md.S. Anwar [c], B. Eggert [d], M.-A. Mawass [e,1], F. Kronast [e], H. Wende [d], R. Bali [c], T. Thomson [a]

[a] NEST Research Group, Department of Computer Science, The University of Manchester, Oxford Road, Manchester, M13 9PL, United Kingdom
[b] National Graphene Institute, The University of Manchester, Oxford Road, Manchester, M13 9PL, United Kingdom
[c] Helmholtz-Zentrum Dresden – Rossendorf, Institute of Ion Beam Physics and Materials Research, Bautzner Landstr. 400, 01328 Dresden, Germany
[d] Faculty of Physics and Center for Nanointegration Duisburg-Essen (CENIDE), University of Duisburg-Essen, 47057 Duisburg, Germany
[e] Helmholtz-Zentrum Berlin für Materialen und Energie, 12489 Berlin, Germany

ARTICLE INFO

Keywords:
Magnetic thin films
Magnetic patterning
Implantation/irradiation
Magnetic domains
Magnetic phase transition

ABSTRACT

Nanoscale magnetic patterning can lead to the formation of a variety of spin textures, depending on the intrinsic properties of the material and the microstructure. Here we report on the spin textures formed in laterally patterned antiferromagnetic (AF)/ferromagnetic (FM) thin film stripes with a period of 200 nm (100 nm FM/100 nm AF). We make use of the AF to FM phase transition in FeRh thin films at ~100 °C, thereby creating a nanoscale pattern that is thermally switchable between AF/FM stripes and uniformly FM. A combination of spin-resolved photoemission electron microscopy, magnetic force microscopy, and magnetometry measurements allow direct nanoscale observations of the stray magnetic fields emergent from the nanopattern as well as the underlying magnetisation. Our measurements reveal pinning centres resistant to temperature cycling that govern the modulated spin-texture as well as a sub-texture consisting of grain-driven nanoscale magnetisation structure directed out of the film plane. The nanoscale magnetic structure is thus strongly influenced by the film microstructure. Signatures of exchange bias are not observed, most likely due to the small contact area between the AF and FM regions, combined with the fact that the interfaces between the damaged and undamaged regions are likely to be highly diffuse owing to the lateral scattering of incoming ions. These results show that temperature controllable spin textures can be created in FeRh thin films which could find application in domain wall, microwave, or magnonic devices.

1. Introduction

The antiferromagnetic (AF) to ferromagnetic (FM) magnetic phase transition (MPT) in equiatomic FeRh in the B2 phase at the technologically useful temperature of ~100 °C has sparked significant research interest in the last decade both to explore the fundamental physics of this coupled phase transition [1–5] and for potential applications [6–9]. A particularly promising use of the MPT in FeRh is in thermally switchable exchange springs, which may be used to enhance heat assisted magnetic recording [8,10]. At the same time, patterning magnetic structures in the nanometre regime by irradiation with light ions opens new avenues for applications, whether it be for storing data in bit patterned media [11,12], spin-orbit torque (SOT) devices [13], domain wall and spin texture racetracks [14,15], magnonics [16], or neuromorphic computing [17]. To enable these applications it is necessary to understand the magnetic behaviour of nanoscale patterned structures. The ability to modify the magnetic structure of FeRh thin films using ion irradiation has now been established [18–24], wherein the irradiation defines regions of distinct magnetic ordering within the FeRh lattice. Depending on the ion irradiation conditions, thin films of FeRh can be modified to remain ferromagnetic over the temperature range of interest or, for higher doses, become paramagnetic [3,20,22,25]. Here we create an FeRh patterned structure consisting of 100 nm wide stripes, with a period of 200 nm, over a large lateral area (8 × 8 mm). Thus, we have a system where one set of wires always responses to magnetic fields (the irradiated FM wires) and the other set to temperature (the unirradiated

* Corresponding author.
E-mail address: william.griggs@manchester.ac.uk (W. Griggs).
[1] Current address: Department of Interface Science, Fritz Haber Institute of the Max Planck Society, Berlin, Germany.

https://doi.org/10.1016/j.actamat.2024.120515
Received 16 April 2024; Received in revised form 15 October 2024; Accepted 25 October 2024
Available online 28 October 2024

AF to FM phase transition wires). The system of interspersed AF and FM wires responds to magnetic fields as well as temperature with the AF to FM modulation vanishing at elevated temperatures. This structure allows us to explore coupling effects and domain structures as a function of thermally controlled magnetisation in a system with well-defined in-plane shape anisotropy. We perform direct observations of the nanoscale magnetisation as well as stray-field configurations at varying temperatures to characterize its complex behaviour.

2. Experimental

A 36 nm thick $Fe_{50}Rh_{50}$ thin film was deposited via dc magnetron sputtering on to a commercial grade (001)-oriented MgO substrate. Details of the sputter deposition parameters, including the pressure, power, annealing temperature and time, can be found in our previously published work [1,6,10,22]. A 500 nm positive resist was applied to the film surface and stripes with 100 nm width and 200 nm period were patterned by electron beam lithography (EBL) using a Vistec EBPG 5000+ electron-beam writer. The patterned area comprised a square of side length 8 mm, leaving an unpatterned border of 1 mm on the 10 × 10 mm substrate. The patterned film was irradiated with Ne^+ ions using a 1090–50 ion implanter (Danfysik A S^{-1}, Taastrup, Denmark), with irradiation parameters calibrated to generate ferromagnetic ordering uniformly through the depth of the film, following our previous work [22]. Ne^+ ions were accelerated to an energy of 25 keV under vacuum (2×10^{-6} mbar). The irradiating ion beam of 10 mm diameter was rastered over the sample at a rate of 1 kHz, subjecting the film to a fluence of 7.5×10^{13} ions cm^{-2} in four minutes, corresponding to a beam current of 60 nA cm^{-2}. The resulting distribution of ion energy deposition was calculated using the Stopping and Range of Ions in Matter (SRIM) code [26].

The film was characterised by X-ray diffraction (XRD), X-ray reflectivity (XRR), and vibrating sample magnetometry (VSM) to confirm the expected crystal structure, layer structure, and magnetic phase transition are present in these samples. The X-ray measurements (see supplementary material) were conducted using a Rigaku SmartLab diffractometer with a one-dimensional D/teX Ultra 250 detector and either a two-bounce Ge(220) monochromator (for XRD) or 5° Soller slits (for XRR). The goniometer step size was $2\theta = 0.01°$. The FeRh layer thickness, density, and roughness were confirmed by fitting a simulation to the measured data using GenX [27], from which the scattering length density (SLD) profile was obtained (supplementary Fig. S1 d. and e.). Crystallographic ordering in the B2 phase was confirmed by the observation of FeRh (001) and (002) XRD peaks (supplementary Fig S1 a.-c.). Variable temperature VSM measurements parallel and perpendicular to the axis of the stripes were conducted using a MicroSense Model 10 magnetometer. Magnetisation vs. applied field data were normalised to the sample volume using the thickness as measured by XRR. Background correction was performed by subtracting linear fits to the high field diamagnetic response.

To understand the effects of irradiation on the magnetic structure of the film, magnetic force microscopy (MFM) measurements were conducted over a range of sample temperatures using a Bruker Dimension Icon scanner in conjunction with a Bruker NanoScope V controller. MFM allows the stray field above the sample surface to be imaged with high spatial resolution, typically on the order of a few tens of nanometres [28]. The probe used was a Bruker MESP-V2. Temperature setpoints were chosen according to a known calibration curve to compensate for the small distance between thermocouple and sample surface. At each temperature setpoint the system was allowed to equilibrate for several minutes prior to measurements being made. All MFM data were acquired over (5.5 × 5.5) μm areas with 272 lines, a scan rate of 1 Hz, and a lift height of 15 nm. Between each successive image, *x* and *y* piezo offsets were adjusted to account for sample drift during temperature cycling, which was monitored by tracking the sample topography.

To complement the MFM measurements, which provide insight on the out-of-plane component of the stray field, we also conducted high-resolution X-ray magnetic circular dichroism photoemission electron microscopy (XMCD-PEEM) imaging. Contrast in XMCD-PEEM images results from the in-plane component of the magnetisation along the incident X-ray beam. Thus, combining this technique with MFM allows us to build a comprehensive picture of the magnetic structure within the embedded wires. The XMCD-PEEM was conducted using the Spin-resolved Photo Emission Electron Microscope (SPEEM) at the BESSY II storage ring in Berlin [29]. This end station comprised an Elmitec III instrument permanently attached to an undulator beamline with full polarization control in an energy range from 80 eV to 2000 eV. The X-ray beam was tuned to the L_3 resonance of Fe at 707 eV and images were recorded under incidence of positive and negative X-ray helicity. In XMCD-PEEM, photoelectrons are generated due to excitation from the 2p core levels of Fe to the exchange-split 3d band. From selection rules the process is spin-selective and dependent on the helicity of the incident photon, resulting in spin-polarized photoemission. Secondary electrons emitted from within a 5 nm depth of the surface are collected by applying a potential of up to 20 kV before being directed onto a multi-channel plate detector. The pixel intensities under the two helicities, I_+ and I_-, are individually averaged and the magnetic contrast image is obtained via $(I_+ - I_-)/(I_+ + I_-)$. The sample temperature was controlled using a heating coil and a liquid He cooling. The red/blue contrast in the resulting images is indicative of the magnetisation being parallel/anti-parallel to the incident X-Ray beam. Non-magnetic features which give no XMCD contrast are used for drift correction and the lateral resolution of the measurement is typically better than 25 nm.

To better understand the MFM and XMCD-PEEM data, we performed micromagnetic simulations of the FeRh nanowires using MuMax3 [30]. The simulation grid consisted of 3000 × 500 × 40 cells with a cell size of 2 nm × 2 nm × 1 nm correspondingly. The simulation geometry comprised five 6 μm × 100 nm × 40 nm wires with a pitch of 200 nm. Periodic boundary conditions were imposed in the *x* and *y* directions. To model the effect of lateral scattering of the irradiating ions, the wires were broadened to 120 nm in width at halfway through their depth. The saturation magnetisation was set to $M_s = 1145$ emu cm^{-3} (from the VSM measurements), the exchange constant was $A_{ex} = 7.5 \times 10^{-7}$ erg cm^{-1} [31]. For the magnetocrystalline anisotropy constant K_1, the literature does not agree on a single value for FM FeRh, with calculated and measured values ranging from 1.3×10^5 erg cm^{-3} [32] to 2.7×10^6 erg cm^{-3} [33]. It has been shown that K_1 in FeRh varies sensitively with lattice strain [34], which makes it particularly difficult to predict in our system where epitaxial strain is mixed with induced disorder. We therefore assumed a value approximately in the middle of the reported range of $K_1 = 1 \times 10^6$ erg cm^{-3}. To account for FeRh polycrystallinity, the magnetocrystalline anisotropy and exchange parameters were varied by up to 10 % over a 2D Voronoi tessellation grain structure with an average grain size of 40 nm [35].

3. Results

The thickness, roughness, density, and crystallinity of the as-grown FeRh films were confirmed by X-ray reflectivity (XRR) and X-ray diffraction (XRD) measurements on the as-grown sample. The XRR data (supplementary Fig. S1 d. and e., with fitting parameters in Table S1) indicates that the FeRh has a thickness of (35.8 ± 0.3) nm and a density of $\rho_{FeRh} = (0.03519 \pm 0.0002)$ f.u. $Å^{-3}$, equivalent to (9.28 ± 0.05) g cm^{-3}, which is within 5 % of the bulk value [3]. Peak intensities measured using XRD give the order parameter $S \approx 0.84$, indicating a high degree of B2 ordering [36] (supplementary Fig. S2). Fig. 1a. illustrates the irradiation process, wherein the Ne^+ ions define stripes of FM ordering in the FeRh film. SRIM simulations of the ion irradiation are shown in Fig. 1b. To model the effects of scattering beneath the resist mask, the simulations include a region in which incident ions are completely blocked from entering the film. The data show that the ions penetrate through the whole depth of the film, with a lateral scattering of up to 10 nm beneath the resist mask. The distribution of displacements per atom

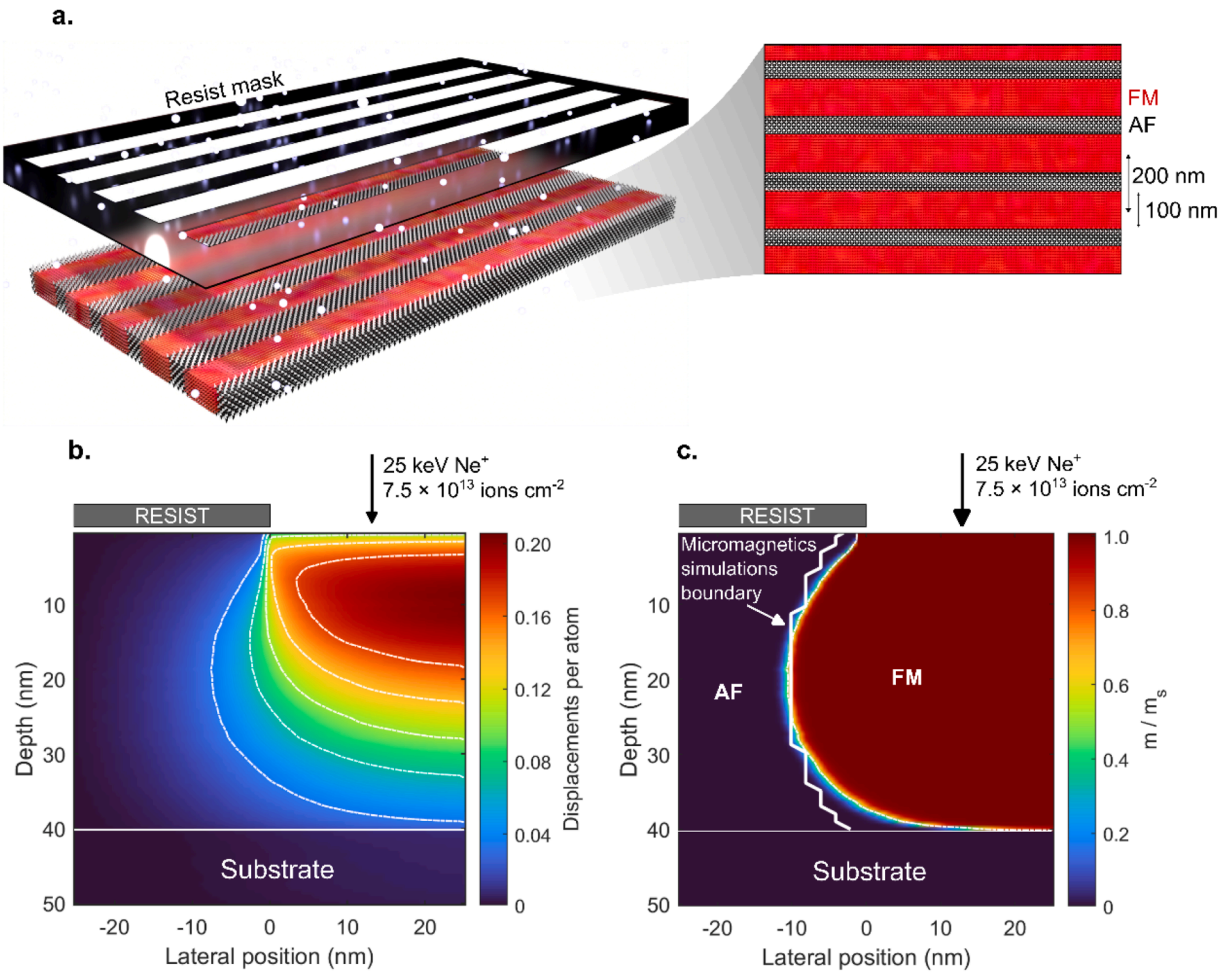

Fig. 1. **a.** Three-dimensional representation of the irradiation of an FeRh thin film through a lithographically patterned resist mask, with complementary plan view. The irradiated regions, which have a width of 100 nm, become uniformly FM at room temperature throughout the film depth. They have a periodicity of 200 nm. The unirradiated regions are AF at room temperature. **b.** SRIM simulations of the displacements per atom as a function of both lateral position under the resist mask and of depth through the FeRh film. The incident ions cause damage throughout the film depth, with an appreciable effect directly beneath the resist mask due to lateral scattering. The dashed lines show constant dpa contours. **c.** Anticipated magnetic moment of the FeRh film resulting from the damage profile calculated in b. The FeRh is uniformly magnetised in the exposed regions, with a 10 nm broadening at the midpoint of the depth (leading to an overall broadening of the stripes by 20 nm halfway through their depth). Also shown is the shape of the wire boundaries in the micromagnetic simulations.

(dpa) in Fig. 1b. can be used to estimate the corresponding magnetisation distribution [22]. The dependence of the measured M_s on the ion fluence observed on continuous, unpatterned films is fitted using an increasing s-curve for the AF/FM to paramagnetic transition. This gives a semi-empirical equation (see Supplement of [22]) which relates the magnetisation to induced atomic displacements i.e., m(dpa). The decaying magnetisation at higher ion-fluences has been considered, but these are negligible for conditions used in this work. The known m(dpa) is applied to the dpa-distribution in Fig. 1b., giving the lateral as well as depth distribution of m, as shown in Fig. 1c. The simulated distribution of Ne^+ ions within the FeRh film after irradiation is shown in Fig. S3 of the supplementary information. The effect of any residual Ne^+ ions is expected to be negligible, as throughout the film depth the concentration remains below one Ne^+ ion per 4000 atoms. This concentration is expected to reduce further as the smaller Ne atom escapes the FeRh lattice. Moreover the Ne atom is unlikely to affect the concentration of itinerant electrons, thereby having a negligible effect on the magnetisation.

The magnetic properties of the patterned FeRh film were characterised by vibrating sample magnetometry (VSM). In-plane hysteresis loops parallel and transverse to the axis of the wires were obtained at a series of constant temperatures from 25 °C to 250 °C (Fig. 2a–g). The 25 °C measurement reveals that the irradiated portions of the film contribute ~370 emu cm^{-3} (normalised by the entire film volume) to the magnetisation $\boldsymbol{M}$ at room temperature. This value is reduced compared to the value reported for bulk FeRh [37], however it is approximately consistent with typical values of ~800 emu cm^{-3} reported in a number of thin film studies [1,20,21,38], given that half of the total volume is expected to be ferromagnetic. The effect of the patterning is manifest in the substantial in-plane magnetic anisotropy seen in the loops taken parallel and transverse to the axis of the wires. FeRh does not usually exhibit a uniaxial in-plane anisotropy; this is therefore solely attributed to shape anisotropy from the patterning. Note that the hysteresis loop does not indicate the presence of any exchange bias between the AF and FM phases, which are in close physical proximity. This observation can be explained by the small contact area between the AF and FM regions, as well as the polycrystallinity of the film likely leading to a broad distribution of Néel vectors within the unirradiated AF regions.

On heating the sample, $\boldsymbol{M}$ increases and loops acquired along both in-plane directions become narrower as the unirradiated regions of the film undergo the temperature-induced MPT. The anisotropy as a function of temperature is given in Fig. 2h., where the area method was used. The data reveal that the uniaxial anisotropy vanishes as the film undergoes the MPT, and remains effectively zero up to the maximum measured

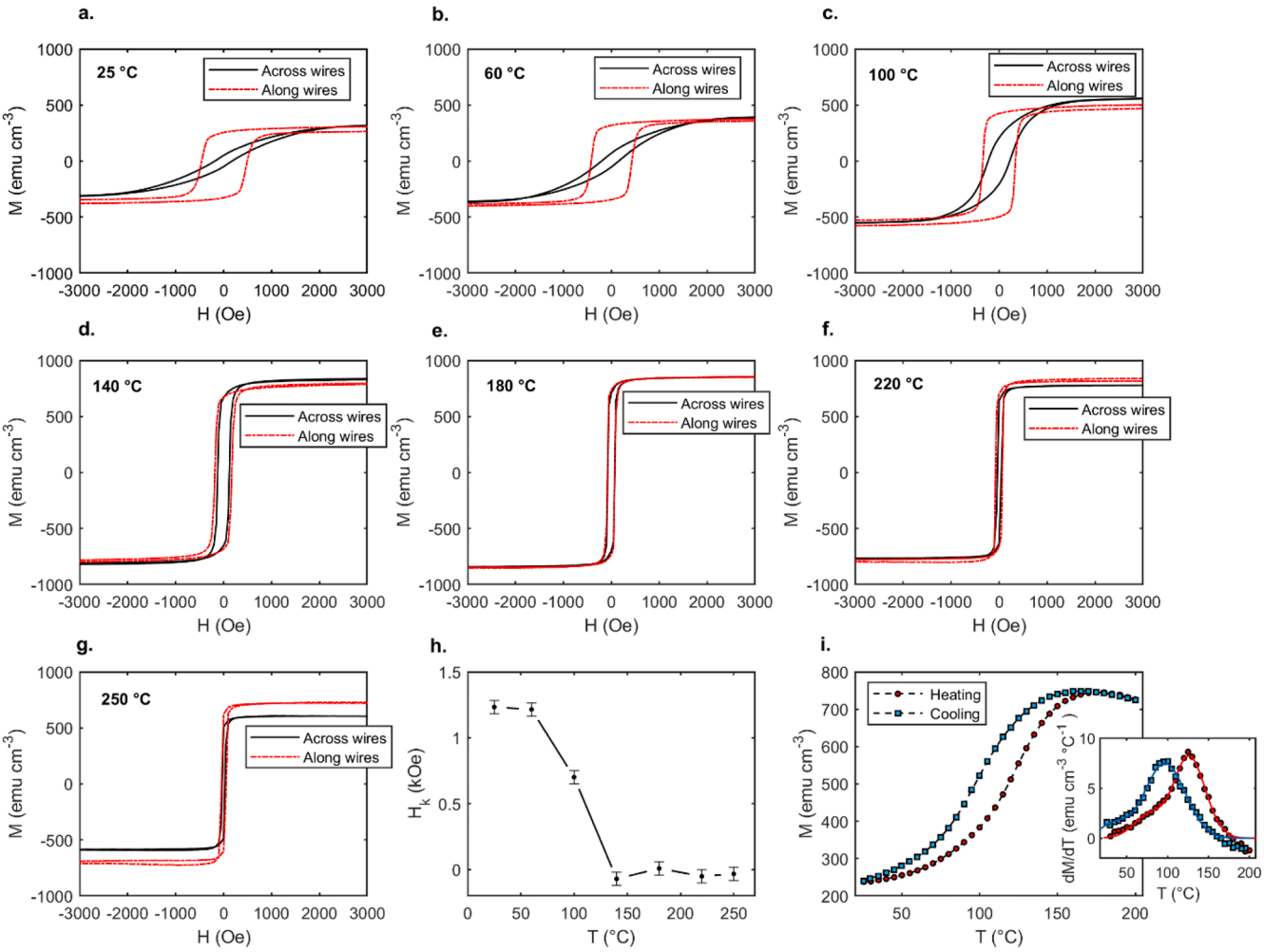

Fig. 2. a. – g. Hysteresis loops measured along and across the patterned stripes at various temperatures. There is a significant in-plane uniaxial anisotropy at room temperature owing to the magnetic contrast defined by the irradiated regions. On increasing the temperature, this anisotropy diminishes and the total moment increases as the unirradiated regions undergo the MPT to FM ordering. The minor discrepancy in saturation magnetisation observed for the 250 °C data across the wires can be attributed to a small calibration error. The data are included as they demonstrate that there is no significant change in anisotropy for the highest temperature. **h.** The anisotropy field H_k as a function of temperature, measured from the data in a. – g. The anisotropy decreases as the MPT progresses. i. Magnetisation under 1 kOe applied field along the stripe axis as a function of temperature, showing the MPT of the unirradiated regions. The inset shows the differential of this data, allowing the MPT temperature to be quantified as $T_{AF\text{-}FM} = 125$ °C.

temperature of 250 °C. This behaviour is consistent with unirradiated regions transitioning from the AF to the FM phase, with the irradiated regions experiencing only a slight reduction in M_s. Indeed, magnetisation vs. temperature measurements on an unpatterned film irradiated by 7.5×10^{13} ions cm^{-2} (Supplementary Fig. S2) show that from 25 °C to 200 °C the magnetisation only reduces by 28 %, as expected far from the Curie temperature. Hence, on heating through the magnetic phase transition, the patterned film becomes uniformly ferromagnetic.

Fig. 2i. shows an ***M*** vs. temperature loop measured at constant in-plane field of 1 kOe. The data show that on heating, the unirradiated portions of the film undergo the MPT, with the total magnetisation increasing by ~500 emu cm^{-3} (normalised by the entire film volume). The phase transition temperature $T_{AF\text{-}FM}$ can be characterised by the peak of dM/dT vs. T (inset to Fig. 2i), which in this case yields a value of $T_{AF\text{-}FM} = 125$ °C.

To characterise the magnetic structure at the nanoscale, magnetic force microscopy (MFM) images were acquired as a function of temperature. Fig. 3 shows the evolution of the magnetic structure as the temperature increases from 24 °C (Fig. 3a) to 160 °C (Fig. 3b). MFM scans at intermediate temperatures in this range are provided in Fig. S4 of the supplementary information. The MFM measurements are sensitive to the out-of-plane stray field at a fixed height of 15 nm above the surface of the sample. Fig. 3c. shows the phase of the oscillating cantilever averaged over the y-coordinate (along the wires) as a function of the x-coordinate (across the wires) for MFM measurements at several temperatures, while Fig. 3d. shows the absolute value of the Fourier transforms of the phase information. The averaged phase and Fourier transformed data are also provided alongside their corresponding MFM images in Fig. S4 of the supplementary information. All MFM data were obtained with a constant out-of-plane magnetic field of 1.5 kOe which is a feature of the thermal measurement stage used.

The MFM images provide a direct visualisation of the AF to FM switchability of the embedded stripes. The AF regions merge into the FM lattice as the temperature increases, then re-emerge as the sample is cooled. The Fourier transforms of the phase data clearly demonstrate a well-defined periodicity, with peaks at 5 μm^{-1} commensurate with the 200 nm pitch of the patterned wires. The spectral data also feature prominent second harmonic peaks at 10 μm^{-1}. For both harmonics the FFT peaks are suppressed on heating of the sample and are recovered on cooling, as shown in Fig. 4a., which plots the reciprocal of the spectral component at 5 μm^{-1} as a function of temperature. The variable temperature magnetometry data of Fig. 2i. is also provided in Fig. 4a. for

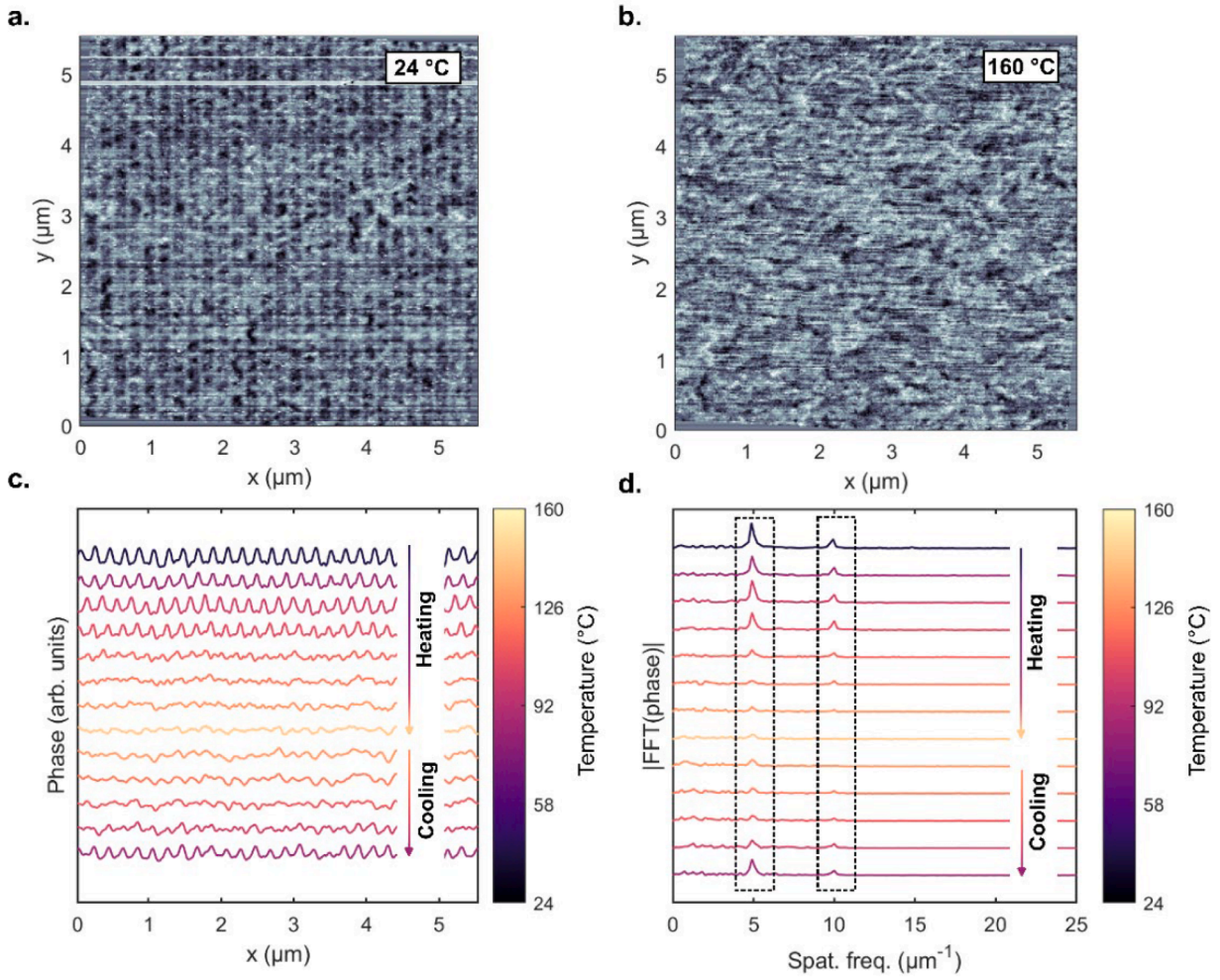

Fig. 3. **a.** MFM image acquired from the sample under a 1.5 kOe out-of-plane magnetic field at 24 °C. The lift height was 15 nm. The irradiated stripes are clearly visible, resulting from modulations in the stray field above the FM regions. **b.** MFM image acquired from the same position on the sample surface as in a., now at 160 °C. The periodic modulations have vanished as the AF regions either side of the FM stripes undergo the MPT. **c.** Cantilever phase data averaged over the *y* coordinate (along the stripes) as a function of the *x* coordinate (across the stripes). The data were acquired over a range of sample temperatures. **d.** Magnitudes of fast Fourier transforms (FFT) of the *y*-averaged phase data from c., where prominent first and second harmonic terms at 5 μm^{-1} and 10 μm^{-1} respectively (inside the dashed boxes) signify the prevalence of the stray field periodicity. These peaks vanish on heating to 160 °C, then re-emerge on cooling.

comparison.

Examining the MFM data in more detail, it is apparent that the magnetic domain structure within the FM wires is unaffected by a heating and cooling cycle. For example, MFM images taken at 80 °C on heating and cooling are well-correlated, as shown quantitatively in Fig. 4c., which provides the two-dimensional cross-correlation of these two images. This analysis shows the similarity between pixel brightness values in the two images as a function of displacement of one of the images; a detailed illustration of this operation is provided in Fig. S5 of the supplementary information. The data feature an intense peak at close to the middle pixel (pixel 270). For comparison, Fig. 4b. shows the cross-correlation between the 80 °C (heating) image and the 160 °C image, which shows no such peak. The similarity between the domain structures in the 80 °C heating and cooling images is made more obvious by presenting the images with a different colourmap, as shown in Fig. S6 of the supplementary information. To demonstrate this comprehensively and quantitatively, cross-correlation plots between all heating and cooling scans are provided in Fig. S7 of the supplementary information. These data evidence that the formation of the domain structure within the FM wires is not driven by thermal effects alone, which would be expected to produce randomized domain formation on repeated thermal cycling. Instead, the correlations between MFM images before and after heating to 160 °C suggest that the microstructure of the wires plays an important role in determining the formation of the domain state.

To further probe the magnetisation of the embedded FM wires, we also conducted variable-temperature XMCD-PEEM measurements on the sample under zero applied field. Illumination by circularly polarized soft X-rays allows ***M*** to be resolved along the direction of X-ray incidence. In Fig. 5, the X-rays are incident with their projection directed downwards along the vertical axis, and the blue (red) contrast indicates ***M*** parallel (anti-parallel) to the light vector. The patterned stripes are aligned slightly off-axis (by approximately 12°) for the given sample mounting conditions. Similar to the MFM images of the stray field above the sample, ***M*** shows pronounced modulations with a periodicity which matches the patterning. Note that the heating and cooling images were acquired from different locations on the sample surface. To complement the Fourier analysis conducted on the MFM data of Fig. 3, a similar analysis is presented on the XMCD-PEEM data in Fig. S8 of the supplementary information.

To better understand the MFM and XMCD-PEEM images, micromagnetic simulations of the irradiated system were conducted. Fig. 6a. shows the simulated magnetisation for the case of zero applied field. Here, a grain structure has been imposed on the stripes with an average grain size of 40 nm. The simulation shows that the stripes divide into

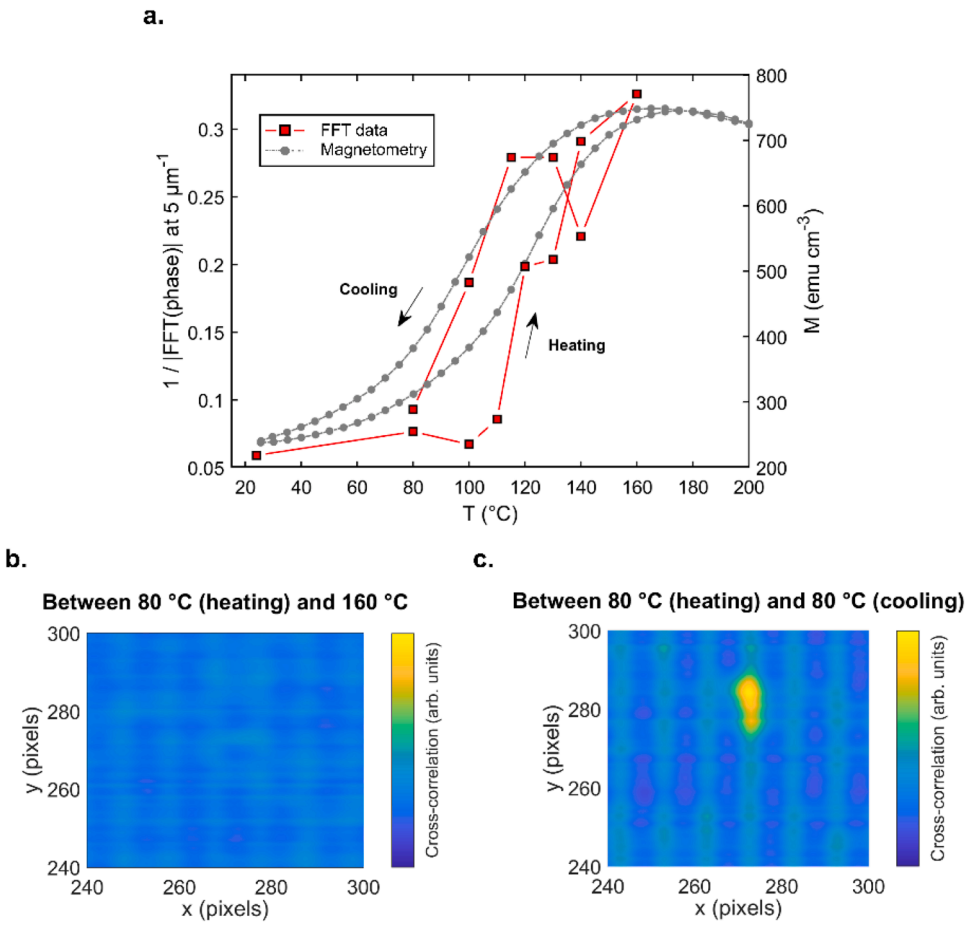

Fig. 4. **a.** The reciprocal of the spectral component of the FFT data at 5 μm^{-1} (Fig. 3d.) is plotted as a function of temperature (red squares, left axis), alongside the thermomagnetic measurements from Fig. 2i. (grey circles, right axis). The reciprocal FFT data show a hysteretic increase with increasing temperature as the AF to FM phase transition progresses. **b.** Cross-correlation plot between MFM data acquired on heating to 80 °C and at 160 °C. There is no discernible correlation. **c.** Cross-correlation plot between MFM images acquired on heating to 80 °C (from room temperature) and cooling to 80 °C (from 160 °C). There is a clear correlation, which is maximal close to the centre of the two images (pixel 270).

antiparallel domains oriented along the stripe axis which are separated by vortex domain walls, with each domain occupying a few microns along the stripe length. To directly compare with the XMCD-PEEM experiment, the component of the magnetisation along the length of the wires is shown in Fig. 6b., which is in good qualitative agreement with the room temperature XMCD-PEEM data of Fig. 5a. Interestingly, repeating the zero applied field simulations without inclusion of a grain structure leads to the stripes being magnetised uniformly along their length, with no vortex domain walls present (supplementary Fig. S9).

In the MFM experiments, the thermal measurement stage used applies a constant perpendicular magnetic field of 1.5 kOe to the sample. Therefore, the simulations were repeated with a 1.5 kOe field applied along the $+z$ direction, with the resulting magnetisation profile shown in Fig. 6c. To account for imperfect alignment of the applied field along the z axis, the applied field in the simulation was given 3 % components in the $+x$ and $+y$ directions. Unlike the zero-applied field case, all the wires become uniformly magnetised predominantly in the $+x$ direction, with a small and spatially varying out-of-plane component. To compare with the MFM data, the magnetisation of Fig. 6c. was converted into a simulated MFM image with an assumed lift height of 50 nm, with the results shown in Fig. 6d. The simulated MFM image is in good agreement with the measured data of Fig. 3a., which was acquired at 24 °C.

4. Discussion

By imaging both the magnetisation and the stray field $\boldsymbol{H}_s$ emanating from a system of embedded FeRh nanowires, we are able to separately identify the effects of temperature, applied magnetic field, and crystallographic defects on the micromagnetic domain structure. For $T < T_{AF\text{-}FM}$, the XMCD-PEEM data show high-aspect domains which span several stripes. While the out-of-plane component of the stray field imaged by MFM shows variations on length scales of ~100 nm, the in-plane component of $\boldsymbol{M}$ observed in the XMCD-PEEM images features domains which occupy several μm along the wire length and several wire widths in the transverse direction. Regardless of the magnetisation direction, the magnitude of $\boldsymbol{M}$ observed in the low temperature XMCD-PEEM images contains microscopic modulations with periodicity matching that observed in by MFM, with well-separated FM (blue and red regions of Fig. 5) and AF (white regions) phases. This is demonstrated quantitatively in the Fourier analysis of Fig. S8 of the supplementary information. In contrast, when $T > T_{AF\text{-}FM}$, the periodic variation vanishes as the AF regions between the wires transform to the FM phase. A direct spatial comparison of the μm-scale domains at different temperatures shows small shifts of the domain boundaries; interestingly however, the approximate size, shape, and position of these domains are largely maintained, even at high temperatures wherein the AF regions have completely transitioned to the FM phase, indicating that domain pinning centres persist at throughout the heating process.

On the other hand, domains observed under stray-field contrast via MFM show nm-scale variations, suggesting that although $\boldsymbol{M}$ is predominantly aligned along the pattern-length, it nevertheless contains microscopic z deviations which result in detectable stray-fields. Despite

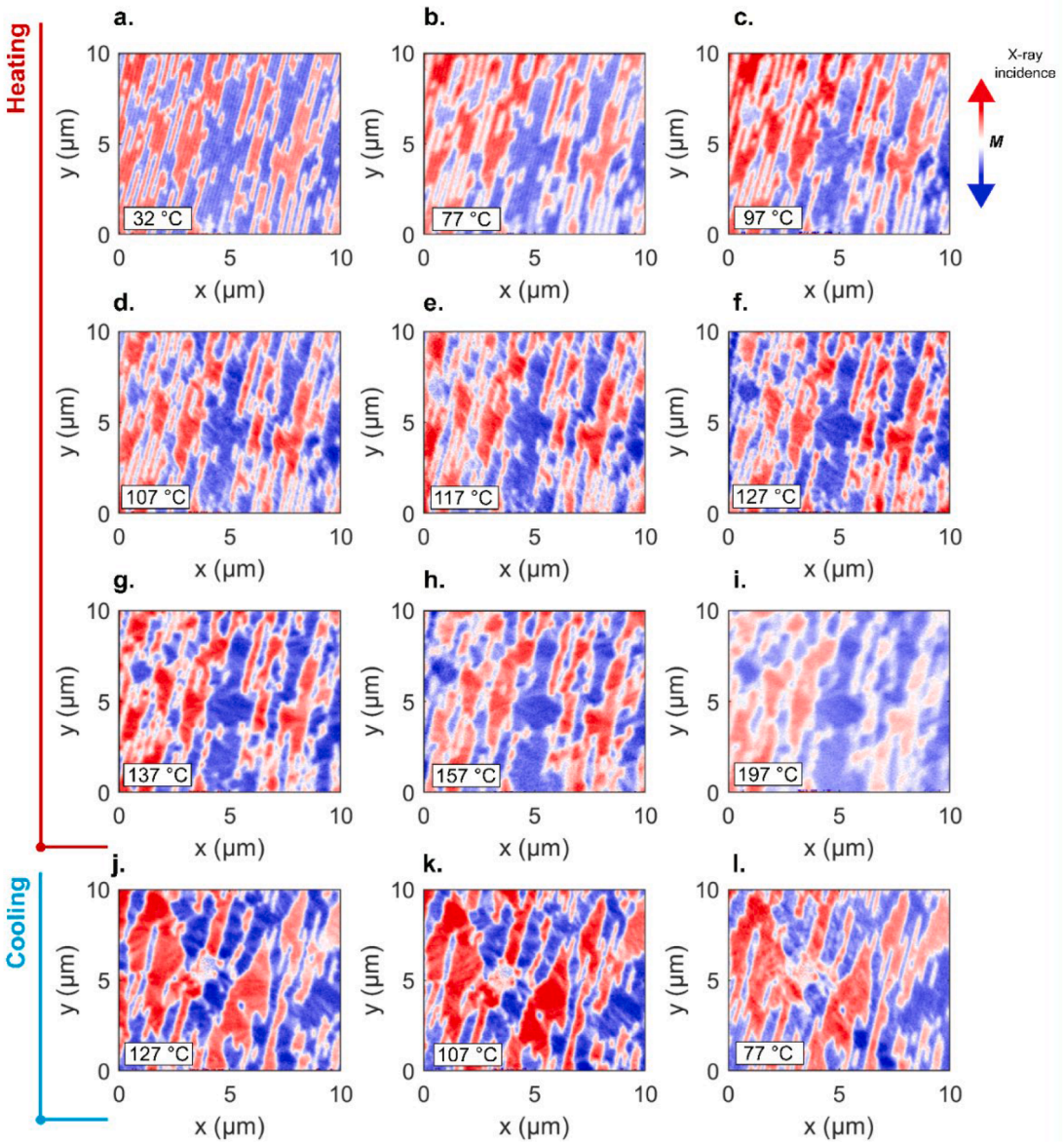

Fig. 5. XMCD-PEEM imaging of the magnetisation vector field ***M***. The contrast mechanism relies on the spin-selective absorption of X-rays at the Fe L_3-edge. The in-plane component of the X-ray wavevector points vertically from top to bottom, and ***M*** is therefore resolved along this direction. The red regions indicate that ***M*** is parallel to the wavevector, while blue shows the antiparallel case. Imaging was done at stabilized temperatures during warming (**a.**-**i.**) and cooling (**j.**-**l.**). Note that the cooling data were acquired from a different location on the sample surface to the heating data.

the presence of these nm-scale deviations, $\boldsymbol{H}_s$ modulations due to the lateral stripe pattern are clear in the FFT data. The combined ***M*** and $\boldsymbol{H}_s$ imaging thus shows that the net magnetisation is aligned along the pattern-lengths and possesses modulations of wavelength 200 nm. There exist local microscopic deflections of the magnetisation away from the length axis, which form nm-scale sub-domains. Under zero applied field, large domains are formed which comprise bunches of magnetic stripes with parallel net-magnetisation over micrometre length scales. These microscopic domains are temperature resistant and are preserved even at elevated temperatures where the stripe modulations vanish. Similarly, the small, nm-scale out-of-plane component of the magnetisation is recovered with the same spatial distribution after thermally cycling, suggesting that it is directly correlated to the microstructure of the thin film.

The results of the MFM and XMCD-PEEM experiments at room temperature can be further understood through comparison with the micromagnetic simulations of Fig. 6, which shows the magnetisation in the topmost layer of the simulated system of FeRh stripes. For the case of the zero-field simulations in which there is a grain structure (Fig. 6a. and b) the magnetisation profile is commensurate with that observed during the XMCD-PEEM experiment (Fig. 5a). The fact that similar simulations with no grain structure lead to the stripes being magnetised along a single direction (Fig. S9 of the supplementary information) provides further evidence that the domain structure of the system of embedded FeRh stripes is a sensitive function of the film microstructure. Similarly, the nm-scale deflections of the magnetisation vector towards the out-of-plane direction observed in the MFM and the simulations with a 1.5 kOe applied field can be understood in terms of small changes to the anisotropy across crystalline grain boundaries.

5. Conclusions

We have demonstrated that it is possible to generate ferromagnetic stripes which are embedded in a thermally switchable antiferromagnetic lattice through ion irradiation over a large area. By imaging both the magnetic stray field above the stripes and the in-plane component of

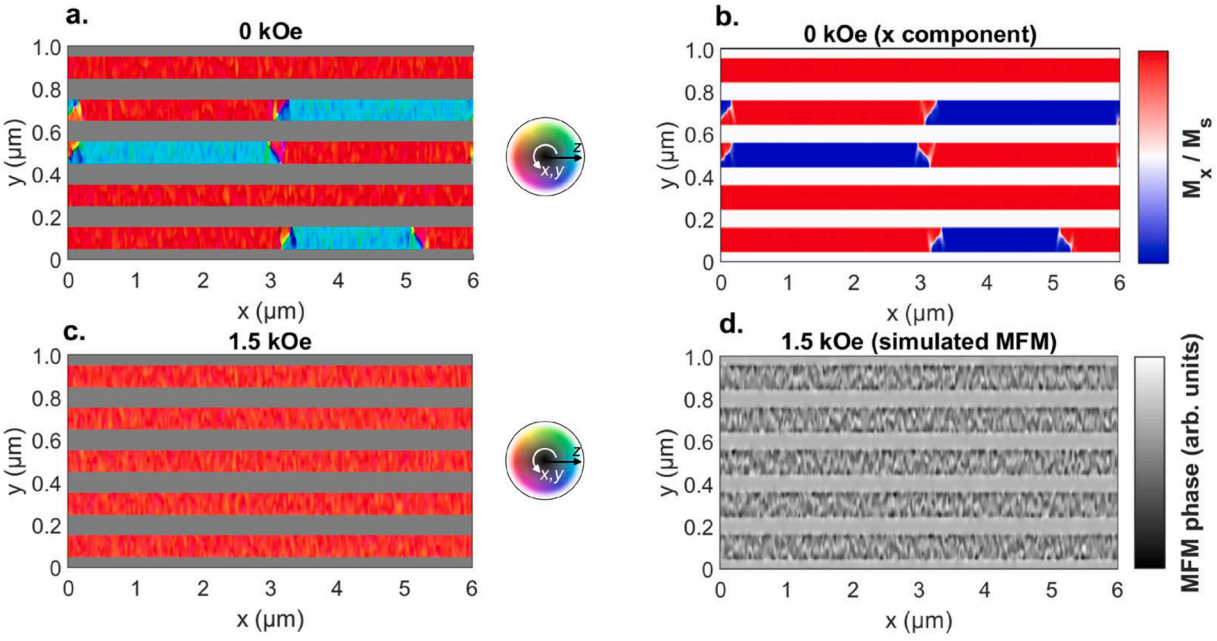

Fig. 6. Micromagnetic simulations of the embedded FM stripes with: **a.** zero applied field, consistent with the XMCD-PEEM measurements, with the component of magnetisation along the length of the wires shown in **b.**, and **c.** a 1.5 kOe field applied perpendicular to the sample, consistent with the MFM measurements. A simulation of the resulting MFM image is provided in **d.**

their magnetisation as a function of temperature, we show that the magnetic periodicity of the irradiated system can be modulated, allowing an in-plane uniaxial anisotropy to be switched on and off. We furthermore show the stripes can be divided into two types of domains. On the one hand, under an out-of-plane applied field each stripe can be separated into regions with distinct out-of-plane components of the magnetisation, which vanish on heating but are fully recovered on subsequent cooling of the sample. The form of this intra-stripe domain pattern is attributed to the microstructure of the irradiated film. On the other hand, under zero field the in-plane component of the magnetisation is separated into antiparallel domains spanning several stripes in width, and this inter-stripe domain state is imprinted on the high-temperature domain pattern in which the stripe periodicity has vanished. Through simulations, we show that the separation of the stripes into antiparallel in-plane domains also results from the film microstructure. Our results demonstrate the potential for the magnetic response of FeRh to be locally tuned for a diverse set of applications, such as in patterned media or switchable mm wave devices, and offer important insight to the magnetic characteristics of such nanoscale magnetic structures.

CRediT authorship contribution statement

W. Griggs: Writing – review & editing, Writing – original draft, Visualization, Validation, Investigation, Formal analysis, Data curation, Conceptualization. **A. Peasey:** Writing – review & editing, Investigation, Formal analysis, Data curation. **F. Schedin:** Methodology, Investigation. **Md.S. Anwar:** Writing – review & editing, Formal analysis, Data curation. **B. Eggert:** Writing – review & editing, Formal analysis, Data curation. **M.-A. Mawass:** Writing – review & editing, Formal analysis, Data curation. **F. Kronast:** Writing – review & editing, Formal analysis, Data curation. **H. Wende:** Writing – review & editing, Formal analysis, Data curation. **R. Bali:** Writing – review & editing, Writing – original draft, Funding acquisition, Formal analysis, Data curation, Conceptualization. **T. Thomson:** Writing – original draft, Project administration, Investigation, Funding acquisition, Formal analysis, Conceptualization.

Declaration of competing interest

The authors declare that they have no known competing financial interests or personal relationships that could have appeared to influence the work reported in this paper.

Acknowledgements

The authors wish to gratefully acknowledge the contribution of the X-ray characterisation facilities of the Henry Royce Institute through EPSRC Grants No EP/S019367/1 and No EP/P025021/1. This work was partially supported by the Impulse-und Net-working fund of the Helmholtz Association (FKZ VH-VI-442 Memriox), and the Helmholtz Energy Materials Characterization Platform (03ET7015). RB and HW acknowledge funding by the Deutsche Forschungsgemeinschaft (DFG) – 322462997 (BA 5656/1–2 | WE 2623/14–2). BE and HW acknowledge the financial support from the Deutsche Forschungsgemeinschaft (Project-ID 405553726-TRR270) and the BMBF (BMBF-Projekt05K2022). XMCD-PEEM Measurements were carried out at the SPEEM instrument at the BESSY II electron storage ring operated by the Helmholtz-Zentrum Berlin für Materialien und Energie (proposal 211–10184-ST). Ion-irradiation was performed at the Ion Beam Centre facility of the Helmholtz-Zentrum Dresden –Rossendorf.

Data availability

All data supporting the findings of this study are available at: https://www.doi.org/10.14278/rodare.3246.

Supplementary materials

Supplementary material associated with this article can be found, in the online version, at doi:10.1016/j.actamat.2024.120515.

References

[1] C.W. Barton, T.A. Ostler, D. Huskisson, C.J. Kinane, S.J. Haigh, G. Hrkac, T. Thomson, Substrate induced strain field in FeRh epilayers grown on single crystal MgO (001) substrates, Sci Rep 7 (2017) 44397.

[2] C. Baldasseroni, G.K. Palsson, C. Bordel, S. Valencia, A.A. Unal, F. Kronast, S. Nemsak, C.S. Fadley, J.A. Borchers, B.B. Maranville, F. Hellman, Effect of capping material on interfacial ferromagnetism, J. Appl. Phys. 115 (2014) 043919.

[3] B. Eggert, A. Schmeink, J. Lill, M.O. Liedke, U. Kentsch, M. Butterling, A. Wagner, S. Pascarelli, K. Potzger, J. Lindner, T. Thomson, J. Fassbender, K. Ollefs, W. Keune, R. Bali, H. Wende, Magnetic response of FeRh to static and dynamic disorder, RSC Adv 10 (2020) 14386.

[4] A.A. Ünal, A. Parabas, A. Arora, J. Ehrler, C. Barton, S. Valencia, R. Bali, T. Thomson, F. Yildiz, F. Kronast, Laser-driven formation of transient local ferromagnetism in FeRh thin films, Ultramicroscopy 183 (2017) 104.

[5] K. Kang, H. Omura, D. Yesudas, O. Lee, K.-J. Lee, H.W. Lee, T. Taniyama, G. M. Choi, Spin current driven by ultrafast magnetization of FeRh, Nat. Commun. 14 (2023) 3619.

[6] W. Griggs, T. Thomson, Repeatable and deterministic all electrical switching in a mixed phase artificial multiferroic, Sci Rep 12 (2022) 5332.

[7] X. Marti, I. Fina, C. Frontera, J. Liu, P. Wadley, Q. He, R.J. Paull, J.D. Clarkson, J. Kudrnovský, I. Turek, J. Kuneš, D. Yi, J.-H. Chu, C.T. Nelson, L. You, E. Arenholz, S. Salahuddin, J. Fontcuberta, T. Jungwirth, R. Ramesh, Room-temperature antiferromagnetic memory resistor, Nature Mater 13 (2014) 367–374.

[8] J.-U. Thiele, S. Matt, E.E. Fullerton, FeRh/FePt exchange spring films for thermally assisted magnetic recording media, Appl. Phys. Lett. 82 (2003) 2859.

[9] R.C. Temple, M.C. Rosamond, J.R. Massey, T.P. Almeida, E.H. Linfield, D. McGrouther, S. McVitie, T.A. Moore, C.H. Marrows, Phase domain boundary motion and memristance in gradient-doped FeRh nanopillars induced by spin injection, Appl. Phys. Lett. 118 (2021) 122403.

[10] W. Griggs, C. Bull, C.W. Barton, R.A. Griffiths, A.J. Caruana, C.J. Kinane, P. W. Nutter, T. Thomson, Polarized neutron reflectometry characterization of interfacial magnetism in an FePt/FeRh exchange spring, Phys. Rev. Mater. 6 (2022) 024403.

[11] C. Chappert, H. Bernas, J. Ferré, J. Kottler, J.-P. Jamet, Y. Chen, E. Cambril, T. Devolder, F. Rousseaux, V. Mathet, H. Launois, Planar patterned magnetic media obtained by ion irradiation, Science 280 (1998) 1919.

[12] T. Kato, D. Oshima, S. Iwata, Ion irradiation for planar patterning of magnetic materials, Crystals 9 (2019) 27.

[13] J. Kurian, A. Joseph, S. Cherifi-Hertel, C. Fowley, G. Hlawacek, P. Dunne, M. Romeo, G. Atcheson, J.M.D. Coey, B. Doudin, Deterministic multi-level spin orbit torque switching using focused He+ ion beam irradiation, Appl. Phys. Lett. 122 (2023) 032402.

[14] R. Juge, K. Bairagi, K.G. Rana, J. Vogel, M. Sall, D. Mailly, V.T. Pham, Q. Zhang, N. Sisodia, M. Foerster, L. Aballe, M. Belmeguenai, Y. Roussigné, S. Auffret, L. D. Buda-Prejbeanu, G. Gaudin, D. Ravelosona, O. Boulle, Helium ions put magnetic skyrmions on the track, Nanno Lett 7 (2021) 2989.

[15] D. Giuliano, L. Gnoli, V. Ahrens, M.R. Roch, M. Becherer, G. Turvani, M. Vacca, F. Riente, Ga+ ion irradiation-induced tuning of artificial pinning sites to control domain wall motion, ACS Appl. Electron. Mater. 5 (2023) 985.

[16] M. Kiechle, A. Papp, S. Mendisch, V. Ahrens, M. Golibrzuch, G.H. Bernstein, W. Porod, G. Csaba, M. Becherer, Spin-wave optics in {YIG} realized by ion-beam irradiation, Small 19 (2023) 2207293.

[17] J. Jadwiszczak, D. Keane, P. Maguire, C.P. Cullen, Y. Zhou, H. Song, C. Downing, D. Fox, N. McEvoy, R. Zhu, J. Xu, G.S. Duesberg, Z.-M. Liao, J.J. Boland, H. Zhang, MoS2 memtransistors fabricated by localized helium ion beam irradiation, ACS Nano 13 (2019) 14262.

[18] D.G. Merkel, G. Hegedűs, M. Gracheva, A. Deák, L. Illés, A. Németh, F. Maccari, I. Radulov, M. Major, A.I. Chumakov, D. Bessas, D.L. Nagy, Z. Zolnai, S. Graning, K. Sájerman, E. Szilágyi, A. Lengyel, A three-dimensional analysis of magnetic nanopattern formation in FeRh thin films on MgO substrates: implications for spintronic devices, ACS Appl. Nano Mater. 5 (2022) 5516–5526.

[19] T. Koide, T. Satoh, M. Kohka, Y. Saitoh, T. Kamiya, T. Ohkouchi, M. Kotsugi, T. Kinoshita, T. Nakamura, A. Iwase, Magnetic patterning of FeRh thin films by energetic light ion microbeam irradiation, Jpn. J. Appl. Phys. 53 (2014) 05FC06.

[20] S.P. Bennett, A. Herklotz, C.D. Cress, A. Levlev, C.M. Rouleau, I.I. Mazin, V. Lauter, Magnetic order multilayering in FeRh thin films by the He-ion irradiation, Mater. Res. Lett. 6 (2018) 106.

[21] C.D. Cress, O. v. '. Erve, J. Prestigiacomo, S.W. LaGasse, A. Glavic, V. Lauter, S. P. Bennett, Domain state exchange bias in a signle layer FeRh thin film formed via low energy ion implantation, J. Mater. Chem. C 11 (2023) 903.

[22] W. Griggs, B. Eggert, M.O. Liedke, M. Butterling, A. Wagner, U. Kentsch, E. Hirschmann, M. Grimes, A.J. Caruana, C. Kinane, H. Wende, R. Bali, T. Thomson, Depth selective magnetic phase coexistence in FeRh thin films, APL Mater 8 (2020) 121103.

[23] A. Iwase, M. Fukuzumi, Y. Zushi, M. Suzuki, M. Takagaki, N. Kawamura, Y. Chimi, N. Ishikawa, J. Mizuki, F. Ono, Study on irradiation-induced magnetic transition in FeRh alloys by means of Fe K-edge XMCD spectroscopy, Nucl. Instrum. Methods Phys. Res. B 256 (2007) 429.

[24] S.P. Bennett, S.W. LeGasse, M. Murrie, O.V. Erve, J.C. Prestigiacomo, C.D. Cress, S. B. Qadri, N+ irradiation and substrate-induced variability in the metamagnetic phase transition of FeRh films, Coatings 11 (2021) 661.

[25] D.G. Merkel, A. Lengyel, D. Nagy, A. Németh, Z.E. Horváth, C. Bogdán, M. A. Gracheva, G. Hegedűs, S. Sajti, G.Z. Radnóczi, E. Szilágyi, Reversible control of magnetism in FeRh thin films, Sci. Rep. 10 (2020) 13923.

[26] J.F. Ziegler, M.D. Ziegler, J.P. Biersack, SRIM - The stopping and range of ions in matter (2010), Nucl. Instrum. Methods Phys. Res., Sect. B 268 (2010) 1818–1823.

[27] A. Glavic, Björck, GenX 3: the latest generation of an established tool, J. Appl. Crystallogr. 55 (2022) 1063–1071.

[28] M.R. Koblischka, U. Hartmann, T. Sulzbach, Improving the lateral resolution of the MFM technique to the 10 nm range, J. Magn. Magn. Mater. 272 (2004) 2138–2140.

[29] F. Kronast, S.V. Molina, SPEEM: the photoemission microscope at the dedicated microfocus PGM beamline UE49-PGMa at BESSY II, Journal of large-scale research facilities 2 (A90) (2016).

[30] A. Vansteenkiste, J. Leliaert, M. Dvornik, M. Helsen, F. Garcia-Sanchez, B. van Waeyenberge, The design and verification of Mumax3, AIP Adv 4 (2014) 107133.

[31] J.R. Massey, K. Matsumoto, M. Strungaru, R.C. Temple, T. Higo, K. Kondou, R.F. L. Evans, G. Burnell, R.W. Chantrell, Y. Otani, C.H. Marrows, Phase boundary exchange coupling in the mixed magnetic phase regime of a Pd-doped FeRh epilayer, Phys. Rev. Mater. 4 (2020) 024403.

[32] X. Zhu, Y. Li, Y. Xie, Q. Qiu, C. Cao, X. Hu, W. Xie, T. Shang, Y. Xu, L. Sun, W. Cheng, D. Jiang, Q. Zhan, Magnetocrystalline anisotropy of epitaxially grown FeRh/MgO(001) films, J. Alloys Compd. 917 (2022) 165566.

[33] C. Bordel, J. Juraszek, D.W. Cooke, C. Baldasseroni, S. Mankovsky, J. Minár, H. Ebert, S. Moyerman, E.E. Fullerton, F. Hellman, Fe spin reorientation across the metamagnetic transition in strained FeRh thin films, Phys. Rev. Lett. 109 (2012) 117201.

[34] G. Zheng, S.-H. Ke, M. Miao, J. Kim, R. Ramesh, N. Kioussis, Epitaxial strain controlled magnetocrystalline anisotropy in ultrathin FeRh/MgO bilayers, AIP Adv 7 (2017) 055914.

[35] J. Leilaert, B. Van de Wiele, A. Vansteenkiste, L. Laurson, G. Durin, L. Dupré, B. Van Waeyenberge, Current-driven domain wall mobility in polycrystalline permalloy nanowires: a numerical study, J. Appl. Phys. 115 (2014) 233903.

[36] C.Le Graët, M.A. de Vries, M. McLaren, R.M.D. Brydson, M. Loving, D. Heiman, L. H. Lewis, C.H. Marrows, Sputter growth and characterization of metamagnetic B2-ordered FeRh epilayers, J. Vis. Exp. 80 (2013) e50603.

[37] L.I. Vinokurova, A.V. Vlasov, N.I. Kulikov, Pressure-induced antiferromagnetism in ferromagnetic {Fe_{51.5}Rh_{48.5}} alloy, J. Magn. Magn. Mater. 25 (1981) 201.

[38] M. Grimes, V. Sazgari, S. Parchenko, J. Zhou, Y. Soh, L.J. Heyderman, T. Thomson, V. Scagnoli, Stabilising transient ferromagnetic states in nanopatterned FeRh with shape induced anisotropy, J. Phys. D: Appl. Phys. (2023).